Meng, F.; Lv, S.; Yang, Q.; Qin, P.; Zhang, J.; Guan, K.; Huang, Y.; Hort, N.; Li, B.; Liu, X.; Meng, J.:

Developing a die casting magnesium alloy with excellent mechanical performance by controlling intermetallic phase.

In: Journal of Alloys and Compounds. Vol. 795 (2019) 436 - 445.
First published online by Elsevier: 04.05.2019

https://dx.doi.org/10.1016/j.jallcom.2019.04.346

Developing a die casting magnesium alloy with excellent mechanical performance by controlling intermetallic phase

F. Meng[1] and S. Lv[1], Q. Yang[2], P. Qin[2,3], J. Zhang[3], K. Guan[2,4], Y. Huang[5], N. Hort[5], B. Li[2,4], X. Liu[2], J. Meng[2]

[1]School of Materials Science and Engineering, Changchun University of Science and Technology, 130022, PR China
[2]State Key Laboratory of Rare Earth Resource Utilization, Changchun Institute of Applied Chemistry, Chinese Academy of Sciences, Changchun 130022, PR China
[3]Key Laboratory of Superlight Materials & Surface Technology, Ministry of Education, Harbin Engineering University, Harbin 150001, PR China
[4]University of Chinese Academy of Sciences, Beijing 100049, PR China
[5]Magnesium Innovation Centre, Helmholtz-Zentrum Geesthacht, Max-Planck-Strasse 1, 21502, Geesthacht, Germany

Abstract

Although Mg-Al-RE (RE: rare earth) alloys have significant weight saving potential in automotive industries, their applications were interrupted due to their unsatisfactory mechanical performance. Intermetallic phases in structural magnesium (Mg) alloys are of practical significance for being able to optimize their microstructures for specific applications. Here we report a new alloy design concept that can develop an alloy for a given system with outstanding mechanical performance and low cost. Such designed alloy exhibits even more excellent strength-ductility balance and cost creep-performance than the commercial/experimental die casting Mg alloys and A380 aluminum alloy. The alloy design concept used in this work is based on strictly controlling intermetallic phase components according to modifying alloy's compositions. Such developed alloy has huge potential to be widely applied in automotive powertrain components acted as the alternative of Mg alloys and even aluminum alloys.

1 Introduction

Magnesium (Mg) alloys having significant weight saving potential have been increasingly attractive in automotive industries for improving fuel economy and vehicle performance attributes [1-5]. Nonetheless, they still remain minimally utilized due to their unsatisfactory mechanical performance compared with the conventional metal materials. It is frequently reported that adding rare earth (RE) elements into Mg alloys improves creep performance and mechanical properties particularly at warm or even high temperatures [2,6-10]. As one representative RE-containing Mg alloy, Mg-4Al-4RE (AE44) alloy was used in the engine cradle of the Corvette [4,11]. Afterwards, numerous research and development (R&D) efforts have led to some degree of improvement on the mechanical performance of AE44 alloy [12-16].

However, its strength or creep resistance still needs to be significantly improved in order to meet the stiffness-limited mass ratio as compared to the next-generation steel, high-strength Al alloys and "high" property carbon fiber/polymer composites [2]. As is well known, the Al-RE intermetallic compounds which mainly distribute at grain boundaries in the Mg-Al-RE-based alloys can effectively impede dislocation motion and grain boundary sliding, thus resulted in high-strength particularly at high temperatures [3,6,17]. Consequently, our research team and other investigators have been paying attention to investigating the influence of single RE element on the dominant intermetallic phases and mechanical properties of Mg-Al-RE-based alloys [18-25]. The results demonstrate that different rare earth elements will result in different intermetallic phase components which further lead to significantly difference on mechanical performance [13,24]. Furthermore, previous literature [22,24] indicates that both alloy's strength and creep resistance clearly decrease as the blocky Al_2RE particles increase in the Mg-Al-Ce, Mg-Al-Nd and Mg-Al-Sm systems. Furthermore, our previous calculations [26] demonstrated that the dominant intermetallic phase tends to be Al_2RE in the Mg-Al-RE system with RE being Y, Sc or those with high atomic numbers such as Ho, Er and Dy. What's more, our experiments indicate that the compositions of Mg-Al-RE (RE = Y, Gd, Ho, Er and Dy) significantly deviate from the designed values due to gathering and precipitation of numerous coarse intermetallic (mainly Al_2RE) particles formed before solidification, and consequently these Mg-Al-RE alloys generally exhibit very low strength particularly at warm and high temperatures. Therefore, taken all RE elements commonly used in Mg alloys into consideration, the Mg-Al-La system was found to have the highest strength and be the most creep-resistant in the Mg-Al-RE systems [12,24]. Microstructural examinations reveal that its dominant intermetallic phase is $Al_{11}La_3$ (body-centered orthorhombic structure, a = 0.443 nm, b = 1.314 nm, and c = 1.013 nm [27,28]) while only few Al_2La particles can be observed in that alloy [24].

According to the above analysis, it is valid to develop an alloy that can provide excellent mechanical performance by regulating RE elements and consequently controlling its intermetallic phase components.

Our current elaborate and systematic work further manifests that for a given alloy system, the intermetallic components can be changed and controlled by strictly controlling the alloy's compositions. Thus, exploring the most excellent mechanical performance for a given alloy system becomes realizable. With respect to the Mg-Al-La system, we found a new intermetallic phase by meticulously controlling the Al/La ratio. Then, we developed a Mg-3.5Al-4.2La-0.3Mn (wt.%) (ALaM440) alloy with Al/La = 0.83 using the high-pressure die casting (HPDC) method, and its intermetallic phase is consisted of such new phase. The newly developed alloy exhibits clearly more excellent strength-ductility balance and cost performance than the currently commercial and experimental HPDC Mg alloys. This alloy design concept, i.e. adjusting and optimizing the intermetallic phase components by strictly controlling alloy's compositions, to develop high-performance materials, is universal for many other alloy systems.

2 Experimental procedures and simulations

2.1 Alloy fabrication

All alloys used in this work were prepared by gravity or HPDC. Pure magnesium and aluminum, Mg-20 wt.% La and Mg-2 wt.% Mn master alloys were preheated to approximately 350 °C for 2 η in a blast furnace. The preheated metals were transferred into a pre-heated steel crucible and melted by electric melting under a protection of continuously flushed CO_2 + 1.2 vol% SF_6 mixed gas. After heated to 740 $\pm$ 5 °C, the melt was stirred for 15 min, and then held for 30 min. Finally, the melt was cooled down to 700 $\pm$ 5 °C with a rate of 1 °C/min. With respect to the gravity die casting samples, the melts were poured into a steel mold (400 x 600 x 32 mm) pre-heated at 250 °C, and then naturally cooled in air. For the HPDC samples, cylindric specimens with the gauge diameter and length of 6 and 60 mm, respectively, were produced using a 380 ton Frech cold chamber HPDC machine. The die was equipped with an oil heating/cooling system with the pre-heated temperature being set to be 250 °C. The alloy compositions for all alloys were determined using an inductively coupled plasma atomic emission spectrum (ICP-AES) apparatus.

2.2 Microstructural characterization

All HPDC samples for microstructural characterizations were cut from the middle segments of cylindric specimens. The samples for XRD were grounded using SiC papers. XRD was carried out using a Siemens diffractometer operated at 40 kV and 40 mA with a Cu (λ = 1.5406 Å) source, and the scanning speed was set to be 0.5 °/ min. The metallographic samples were initially grounded using different grades of SiC paper, and then polished with Al_2O_3 paste. Finally, the polished surface was etched in a solution of acetic picral (5 ml acetic acid + 5 g picric acid + 10 ml distilled water + 90 ml ethanol absolute). The morphologies and distributions of intermetallic phases were characterized by a scanning electron microscopy (SEM) with a JEOL 7001 FEG operated under a Z-contrast backscattered electron imaging mode. Samples for transmission electron microscopy (TEM) were cut with a thickness of 0.5 mm using wire cutting machine. TEM discs with a diameter of 3 mm were punched from these slices. Then, these discs were ground to a thickness of 25 $\pm$ 5 mm and then ion-milled using a Gatan Precision Ion Polishing System in the Ar ion-beam thinning process. Finally, all foils were cleaned to reduce the contamination using a Model 1020 Plasma Cleaner (Fischione Instruments). The bright-field TEM (BF-TEM) observations, selected area electron diffraction (SAED) along with the energy-dispersive X-ray spectrometer (EDS) analysis were performed using FEI Tecnai G2 F20 microscopy. High-angle annular dark field scanning transmission electron microscopy (HAADF STEM) images were got using FEI Taitan3TM G2 60-300 microscopy operated at 300 kV and equipped with two CEOS aberration correctors and a Fischione HAADF detector. The probe convergence was 25 mrad which yielded a probe size of less than 0.1 nm. For clarity, the atomic resolution HAADF STEM images except for those of the interface were Fourier-filtered by masking the corresponding diffraction pattern from the original image and back-transforming using a Gatan Digital Micrograph. To evaluate the volume fraction of the intermetallic phases, all gravity casting alloys were characterized using XRD and TEM. Firstly, the dominant intermetallic phases were identified from the corresponding XRD patterns. Then, the structures of the minor intermetallic phases along with a part of dominant intermetallic phases were revealed using TEM. Finally, based on amounts of TEM observations along with the SAED analysis, the relatively volume fraction of each intermetallic phase in a certain alloy was estimated.

2.3 Diffraction pattern simulation

To identify whether a reflection belongs to a certain phase, Single Crystal (CrystalMaker Software Ltd) [29] was used. With respect to a given crystal structure, both d-spacings and positions of the diffraction spots within an electron diffraction

pattern were simulated. Comparing the simulated patterns with the experimental SAED patterns provides direct clues to find a match. The crystallographic data of various Al-RE intermetallic phases was got from Pearson's Crystal Database [30]. To simulate diffraction patterns under specific zone axes, unit cells were oriented to identical orientations with electron beam.

2.4 HAADF STEM image simulation

Structural modeling and HAADF STEM image simulation were performed using the software package of QSTEM [31]. The η-Al_3La supercell structure model consisting of 10 x 10 x 10 unit cells (44.37 Å x 45.08 Å x 97.72 Å) was used for simulations. The probe array was set as 500 - 500 pixels with a resolution of 0.025 Å. The slice thicknesses were 1.4790 Å, 1.5027 Å and 2.1084 Å for [100], [010] and [110] zone axes, respectively. An area of 40 Å - 70 Å consisting of 250 - 250 pixels was selected for image simulations.

The microscope parameters for QSTEM were as follows: 300 kV high voltage; 3.0 nm defocus; -3 μm astigmatism spherical aberration, C3; 30 mrad convergence angle; 5 - 10^8 brightness (A/cm^{2}sr); TDS on; 0.5 eV dE; 1 ms dwell time; 300 K temperature; 0 deg angle; and 0 deg beam tilt. The values for detector geometry were 60-e300 mrad.

2.5 Density functional theory (DFT) calculation

DFT simulations were carried out using the Vienna ab-initio Simulation Package (VASP 5.2.2) with a plane wave basis [32]. The exchange-correlation energies were evaluated using Perdew-Burke-Ernzerhof (PBE) formulation within the generalized gradient approximation (GGA) [33]. The projector augmented wave (PAW) pseudo-potentials [34,35] were used for all calculations. Convergence tests indicated that 400 eV was a sufficient cutoff for the PAW potential to achieve high precision. Monkhorst Pack integration schemes of 17 x 9 x 11 and 17 x 17 x 11 were used for the integration of the irreducible Brillouin zones of $Al_{11}La_3$ and η-Al_3La, respectively, to ensure that the convergence is in the order of a few meV atom^{-1}.

3 Results and discussion

3.1 Alloy design concept

ALaM440 alloy was designed based on strictly controlling the components of intermetallic phases through controlling alloy's compositions. Fig. 1 gives the

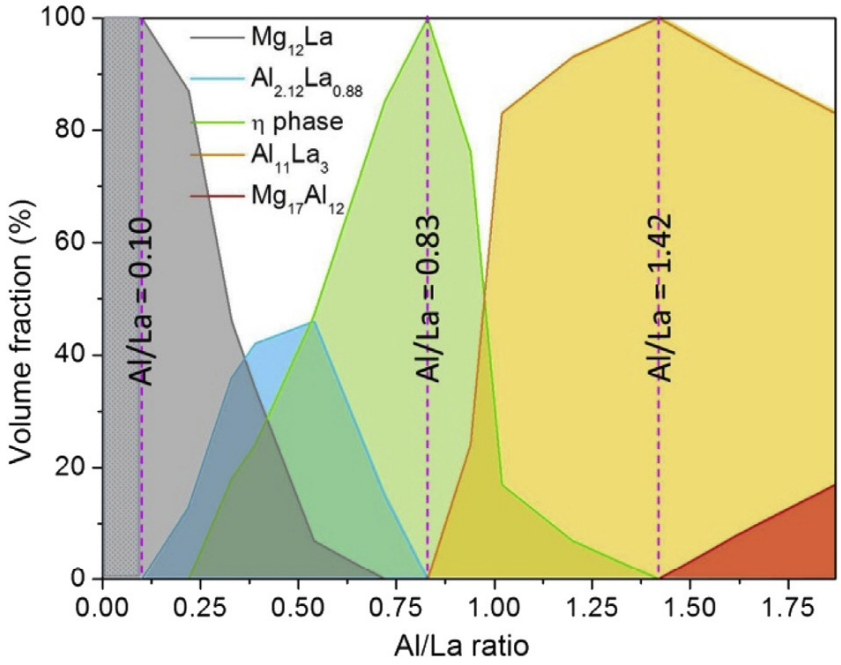

Figure 1: The components of intermetallic phases examined using XRD and TEM in the Mg-4La-xAl (x = 0-8, wt.%) alloys fabricated by gravity die casting. The purple dotted lines correspond to the critical Al/La ratio for the formation of certain simplex intermetallic phase, and the dotted gray area corresponds to the Al/La range where only $Mg_{12}La$ phase forms. (For interpretation of the references to color in this figure legend, the reader is referred to the Web version of this article.)

detected intermetallic phases in a series of Mg-4La-xAl (x = 0-8) (wt.%) alloys fabricated by gravity die casting. When the Al/La ratio is less than approximately 0.10, the intermetallic phase is $Mg_{12}La$, which frequently results in poor ductility and unsatisfactory creep resistance [36,37]. As the Al/La ratio increases, another intermetallic phase, namely $Al_{2.12}La_{0.88}$, forms in the alloys. This phase is unstable and always coexists with other intermetallic phases [38]. When the Al/La ratio is over 0.22, a new intermetallic phase, designated as η phase in this study, forms in the alloy, and becomes the simplex intermetallic phase at Al/La ratio of $\sim$0.83. However, its influence on alloy's mechanical performance still remains blank. As the Al/La ratio continues increasing, the wellknown $Al_{11}La_3$ and $Mg_{17}Al_{12}$ phases successively form. The $Al_{11}La_3$ phase has hitherto been regarded as the most effective intermetallic phase to contribute high strength and excellent creep resistance in the Mg-Al-RE systems [12,13,24], while the $Mg_{17}Al_{12}$ phase, the dominant intermetallic phase in many commercial Mg-Al-based alloys, acts as a delinquent role in the alloys' low strength and rapid creep at warm or high temperatures [6,12,13,39]. Therefore, in order to explore the potential mechanical performance of Mg-Al-La system, investigation dealing with revealing the crystal structure and strengthening effects of η phase is of overwhelmingly important. To ensure that the newly designed alloy has comparable castability with the commercial AE44 alloy, the Al content was selected to be 3.5 wt.%. Then, strictly controlling the Al/La ratio as 0.83, an alloy with nominal compositions of Mg-3.5Al-4.2La-0.3Mn in wt.% was designed and then fabricated by HPDC, and this alloy can be regarded as a variant of the most familiar heat-resistant AE44 alloy.

3.2 Microstructure of ALaM440 alloy

Compositions of the obtained HPDC ALaM440 alloy are Mg-3.51Al-4.16La-0.23Mn (impurities: 0.012 Si, 0.001 Fe, and <0.001 Ni) in wt.%. Fig. 2a shows the typical microstructure of this alloy. The acicular intermetallic particles and mainly distribute at dendritic boundaries. This is highly consistent with the characters of the wellknown $Mg_{17}Al_{12}$ particles in AE44 alloys. However, the corresponding XRD pattern (Fig. 2b) indicates a significant inconformity between the experimental peak positions (inverted triangle) and theoretical diffraction peak positions for $Al_{11}La_3$ (red lines) or Al_2La (green lines). Statistic EDS analysis results suggest a stoichiometry of approximately Al_3La for the acicular phase (Fig. 2c). Subsequently, the η phase in ALaM440 alloy was also marked as η-Al_3La. Furthermore, the obtained SAED patterns (Fig. 2d-g) from the acicular phase cannot be reasonably indexed by any known Al-RE or Mg-RE phases to our best knowledge. Recently, Wong et al. [25] found a new $(Al,Mg)_3La$ phase in a cast Mg-Al-La system. Its reported SAED patterns are highly similar to those presented in Fig. 2d-g. However, the simulated patterns based on the reported

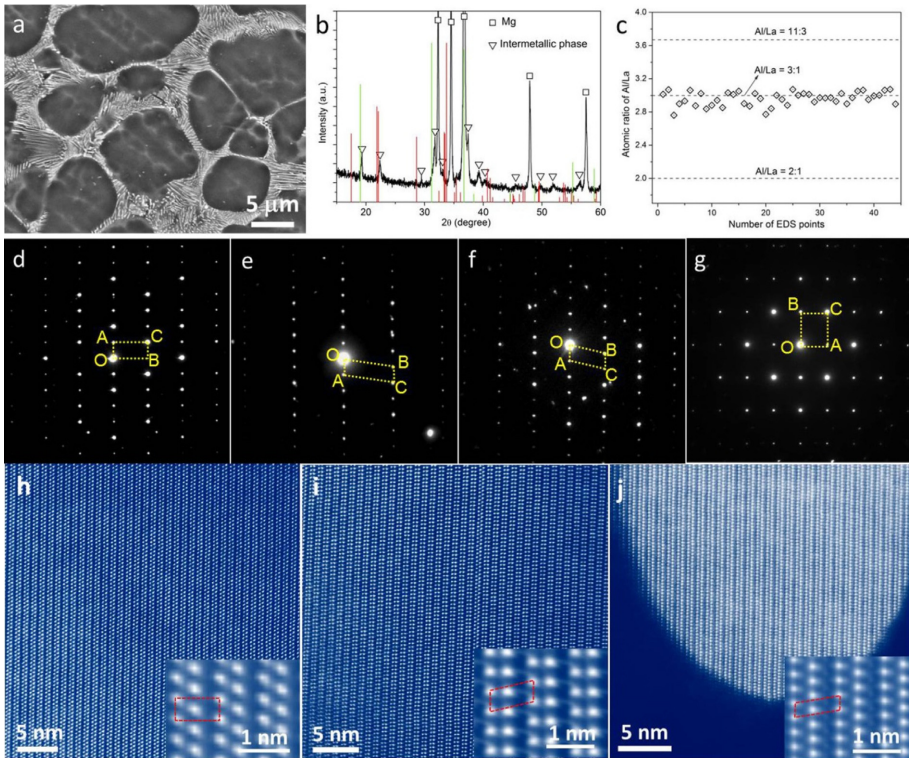

Figure 2: (a) Backscatter SEM image of the studied ALaM440 alloy, (b) the corresponding XRD pattern (the known Al_2La and $Al_{11}La_3$ were indicated by green and red lines, respectively), (c) the statistical diagram of the atomic ratio of Al/La for the new intermetallic phase, (deg) the corresponding SAED patterns on various zone axes for this new phase, and (h-j) HAADF STEM images of the η-Al_3La phase taken along the zone axes indicated by (def) respectively. The insets in (h-j) show the higher magnifications with the unit cell schematically indicated by red dotted parallelograms. (For interpretation of the references to color in this figure legend, the reader is referred to the Web version of this article.)

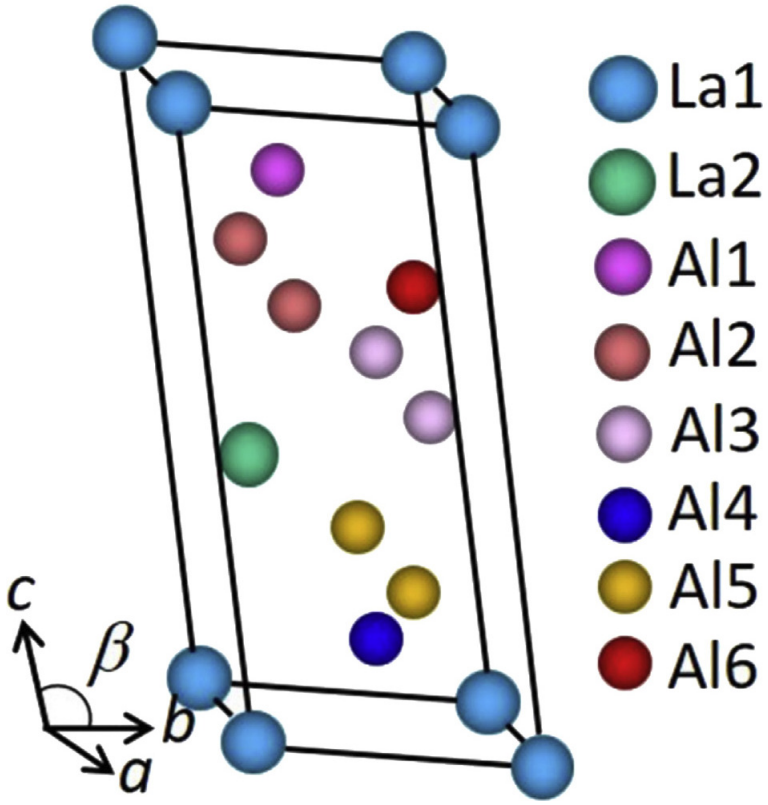

Figure 3: Unit cell configuration of the DFT optimized η-Al_3La phase.

$(Al,Mg)_3La$ structure clearly deviate from the experimental SAED patterns of η-Al_3La (see Supplementary Fig. 1). Therefore, the acicular phase in ALaM440 alloy is not $(Al,Mg)_3La$.

3.3 Crystal structure of η phase

SAED pattern analysis for the η-Al_3La phase were conducted in this work (see Supplementary Fig. 2). The reconstructed three-dimensional reciprocal lattice indicates a monoclinic structure with cell parameters of a = 0.4437 nm, b = 0.4508 nm, c = 0.9772 nm, and β = 103.5°. Additionally, a high resemblance between the simulated $[100]_{\beta-Al_3La}$ pattern and the experimental $[100]_{\eta-Al_3La}$ pattern was found (see Supplementary Fig. 3). Then, the initial atomic configuration of η-Al_3La was built on the basis of that of β-Al_3La, with a schematic process shown in Supplementary Fig. 4. Afterwards, DFT [32] optimizations were performed on the initial η-Al_3La cell. To ensure the accuracy of DFT calculations, the well-known $Al_{11}La_3$ structure was also optimized. The good agreement between our

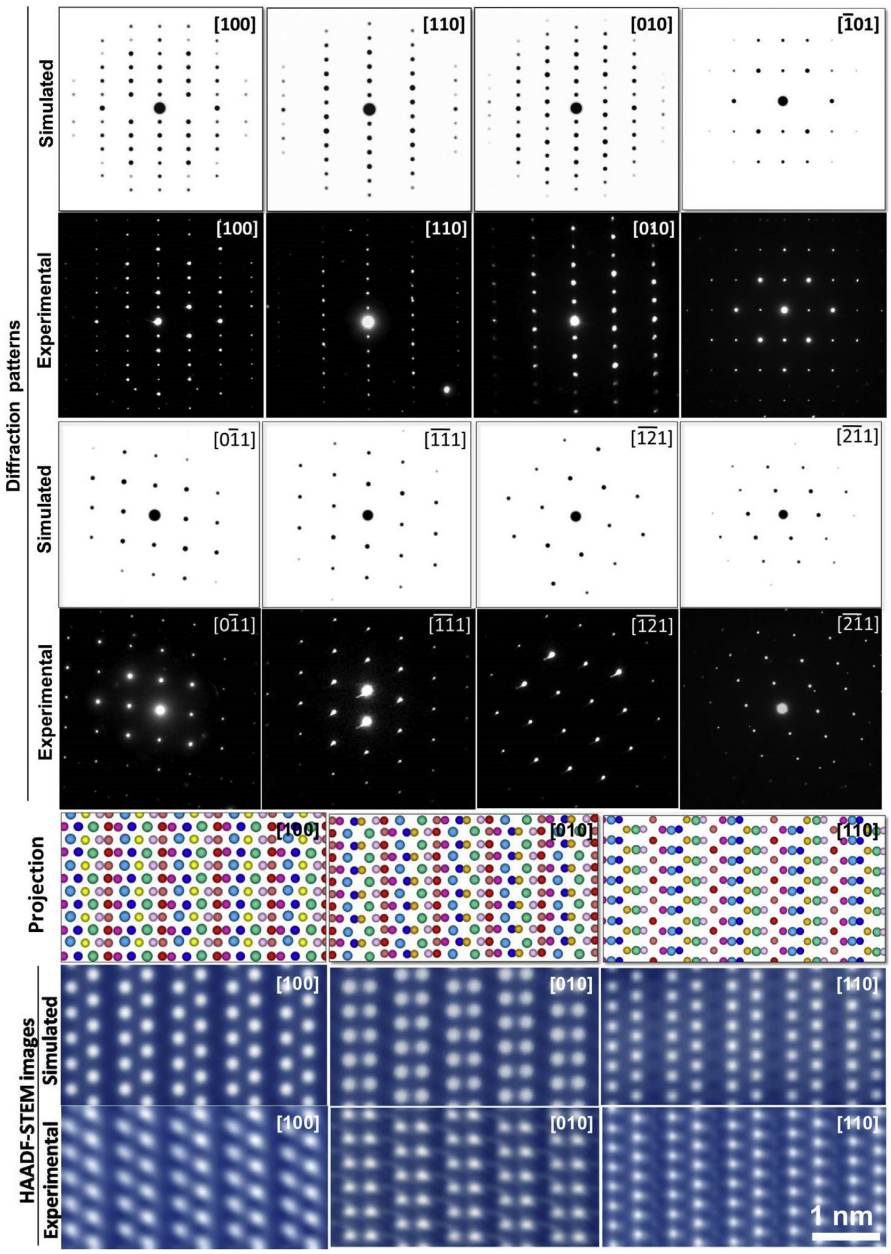

Figure 4: (the first and third rows) The simulated electron diffraction patterns along various zone axes, (the second and fourth rows) the corresponding experimental SAED patterns, (the fifth row) models viewed from [100], [010] and [110], respectively, with the colors of the balls being consistent with those in Fig. 3, (the sixth row) simulated HAADF STEM images using the above models, and (the last row) HAADF STEM images taken from [100], [010] and [110], respectively. (For interpretation of the references to color in this figure legend, the reader is referred to the Web version of this article.)

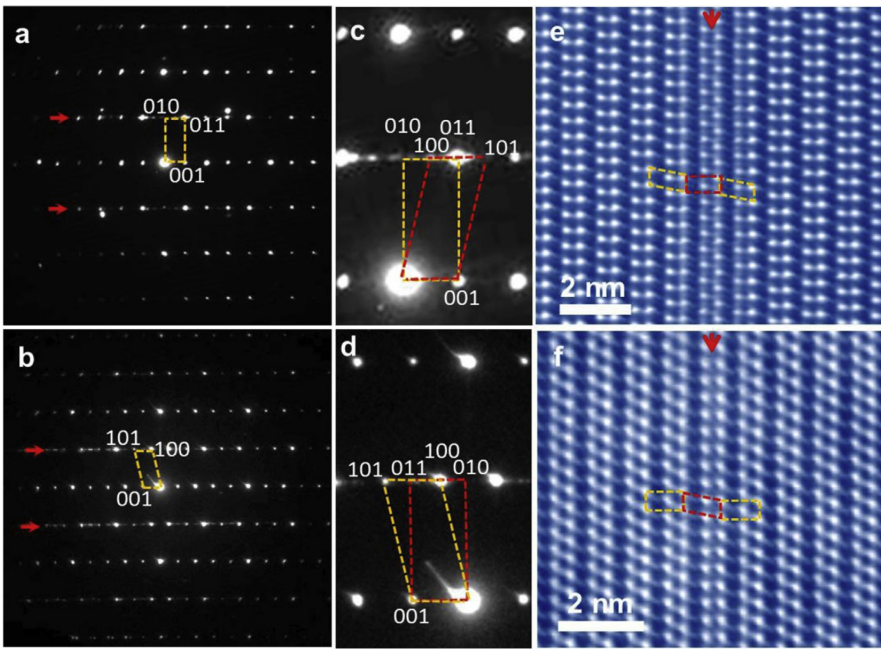

Figure 5: (a) and (b) SAED patterns along [100] and [010] zone axes, respectively, and the corresponding (c and d) magnified SAED patterns and (e and f) atomic resolution HAADF STEM images.

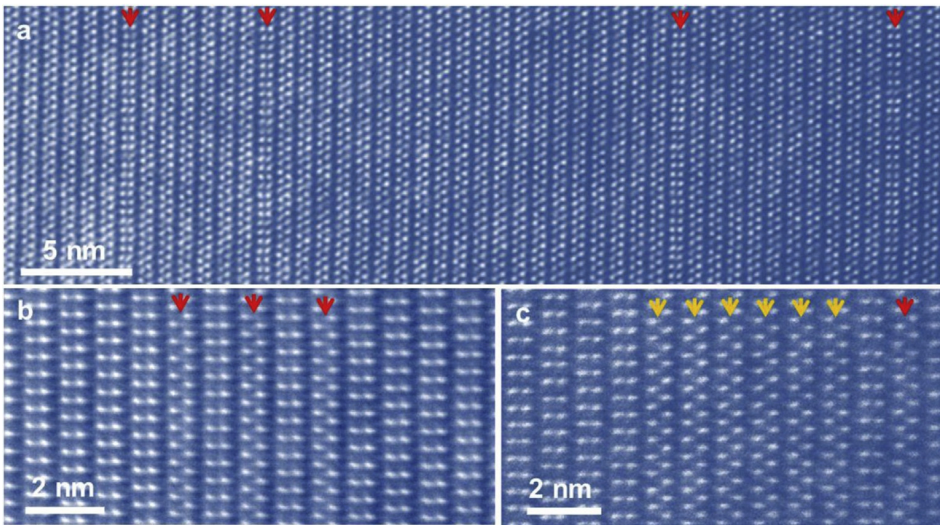

Figure 6: HAADF STEM images with various distributions for MOTs (marked by red arrows) and orientation twin (marked by orange arrows) in η-Al_3La phase. (For interpretation of the references to color in this figure legend, the reader is referred to the Web version of this article.)

calculations and experimental results [27] suggests that the calculation results are credible (see Supplementary Table 1). Fig. 3 displays the optimized atomic configuration of η-Al_3La phase, with its calculated lattice parameters along with the atomic coordinates being tabulated in Supplementary Table 2. The calculated lattice parameters are reasonably agreeable with the experimentally measured ones. Furthermore, the simulated electron diffraction patterns from the optimized η-Al_3La structure are highly consistent with the corresponding experimental SAED patterns (see Supplementary Fig. 5). Finally, both the projections of optimized η-Al_3La structure and the simulated HAADF STEM images elegantly match with the corresponding experimental HAADF STEM images, such as shown in Fig. 4. These results provide strong supports for the accuracy of η-Al_3La structure analysis in the HPDC ALaM440 alloy. Finally, the formation energy of η-Al_3La was calculated to be -0.430 eV/atom, demonstrating that the formation of η-Al_3La is energetically favorable.

3.4 Planar faults within η phase

Planar faults are frequently observed in intermetallic particles and might be important for understanding the ductility of alloys [40-42]. In this work, planar faults were also observed in the η-Al_3La phase (see Supplementary Fig. 5a-f). In the

corresponding SAED patterns from both [100] (Fig. 5a) and [010] (Fig. 5b) incidences, streaking can be identified along the [001]* direction in the [010] and [100] reciprocal lattice rows, respectively (indicated by red arrows). A closer look (Fig. 5c and d) reveals that the streaking can be identified as individual diffraction spots. More interestingly, the extra spots in the [100] pattern correspond to the [010] pattern, and vice versa. Thus, these planar faults in the η-Al_3La phase are not stacking faults but orientation faults, which was generally defined as orientation twin [41]. Atomic resolution HAADF STEM observations (Fig. 5e and f) indicate that this orien-tation fault is always consisted of monolayer η-Al_3La structure with different orientations from matrix. Then, we designated it as monolayer orientation twin (MOT). Generally, the MOTs randomly and discretely distribute in the η-Al_3La phase, with distance between two MOTs (d_{MOT}s) being larger than two layers (Fig. 6a). In some cases, two or more MOTs are uniformly-spaced, with d_{MOT}s being one layer, or hold together and form a well-defined orientation twin (Fig. 6b and c, respectively).

3.5 Mechanical properties and application expectation

Fig. 7a summarizes the yield strength and elongation to failure for various HPDC Mg alloys [6,22,24,43-48] along with the classic HPDC A380 aluminum alloy [6,43,49,50]. Generally, the alloys with higher yield strength have a lower elongation and vice versa. However, the ALaM440 alloy developed in this work exhibits the most excellent strength-ductility balance compared with the previously studied HPDC Mg and A380 alloys. Furthermore, although having slightly lower strength than the HPDC A380 alloy, the ALaM440 alloy exhibits the highest ultimate tensile strength at room temperature in all commercial and experimental HPDC Mg alloys [6,22,24,43-48,51,52] to our knowledge (see Supplementary Fig. 6).

In order to save more weight in automotive powertrain parts, the most important requirements for the alternative alloys are their elevated temperature properties, such as creep resistance [2]. Although HPDC aluminum alloys such as A380 are occupying the dominant market of lightweight die casting powertrain components, Mg alloys are also the technically valid alternatives because they can save more weight. Thus, the cost performance becomes the key factor for Mg alloys to being used in powertrain components. Fig. 7b shows the creep strength versus the cost of traditional HPDC Mg alloys relative to that of the HPDC A380 alloy [4,6,43,44,53,54]. In thermal environments over 150 °C, the ALaM440 alloy developed in this work along with the AXJ530 (Mg-5Al-3Ca-0.07Sr, wt.%) alloy exhibit excellent cost creep-performance in HPDC Mg alloys. However, the ALaM440 alloy owns lower cost, higher strength and ductility balance, and better castability [43] than the AXJ530 alloy. Therefore, the ALaM440 alloy is the most potential Mg alloy to be used for automotive powertrain components. Moreover,

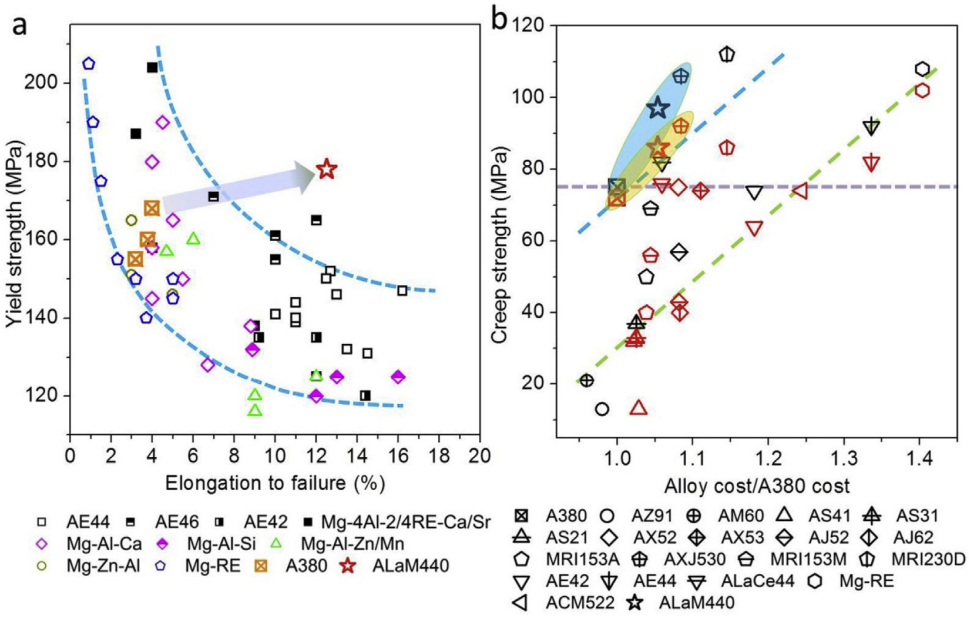

Figure 7: (a) Yield strength and elongation to failure of various HPDC Mg systems along with the A380 alloy [5,19,21,40e47]. Overall, die casting Mg alloys display an inverse relationship between yield strength and elongation, as indicated by the area between two blue dash lines. (b) The creep strength (the stress to produce 0.1% creep strain at 100 h) and the cost of the traditional die casting Mg alloys relative to that of A380 alloy [3,5,40,41,50,51]. The black symbols in (b) stand for the creep strength data at 150 °C while the red ones at 175 °C. The green dash line in (b) stands for the general cost creep-performance line for traditional die casting Mg alloys, and the blue dash line in (b) stands for the tolerant cost creep-performance line compared with the die casting A380 alloy. Thus, the alloys located above the blue dash line are regarded to own more excellent cost creep-performance than A380 alloy, and vice versa. (For interpretation of the references to color in this figure legend, the reader is referred to the Web version of this article.)

the ALaM440 alloy has comparative or even more excellent mechanical properties and cost creep-performance than the HPDC A380 alloy. As a result, such developed alloy in this work would lead to an early acceptance by the user due to its relatively low cost and even more excellent mechanical performance compared with the A380 alloy.

4 Discussion

According to microstructural analysis, the ALaM440 alloy owns comparative cell sizes ($\sim$14 mm) and Al concentration in Mg matrix with those of the reported AE44 alloys. Thus, the η-Al_3La phase possibly contributes to more excellent strength and ductility bal-ance than the $Al_{11}La_3$ phase. Then, since η-Al_3La owns comparable bulk modulus (66.2 GPa) with $Al_{11}La_3$ (69.9 GPa), their resistance to normal strain is thus indiscriminate. In addition, the η-Al_3La phase ordinarily has finer size than the $Al_{11}La_3$ phase. With respect to Orowan dislocation bypassing strengthening, smaller particle size and interparticle spacing would result in higher strength [55]. Therefore, the η-Al_3La phase contributes to higher strength increment than the $Al_{11}La_3$ phase.

According to TEM observations, any eutectic area (EA) with approximately uniform η-Al_3La phase distribution belongs to certain adjacent α-Mg grain (Fig. 8a). As an example, EAI belongs to α-Mg grain I (aI), EAII belongs to aII, and so on. However, the adjacent layered Mg matrixes in EAs frequently stand with a minor misorientation (<3°) (see Supplementary Fig. 7). Furthermore, the η-Al_3La particles at EA/α-Mg boundaries generally stand in the α-Mg grain, not in the EA (Fig. 8b). In Mg polycrystals, both basal and pyramidal slip have to be activated during deformation to satisfy von Mises' criterion that every grain should be able to plastically deform to meet the shape changes imposed by its neighbors [56]. Even in the basal-slip dominated grains, the pyramidal slip would also be activated when the basal dislocations interacted with the acicular η-Al_3La particles. As is well known, deformation along the <c> axis is primarily accomplished by <c + a> = 1/3<1123> dislocation gliding on the pyramidal {1122} planes [56,57]. This dislocation gliding would result in a small orientation change [58]. When <c + a> dislocation gliding in EAs, the misorientation between the layered Mg matrix could slightly decrease the gliding orientation changes, reducing bypassing energy barrier. Then, the interface between η-Al_3La and Mg matrix also plays a key role for the alloy's mechanical performance, since stresses and strains are transferred from matrix to the intermetallic particles via the interface. TEM examinations (Fig. 8c and d) suggest that the η-Al_3La phase is coherent with Mg matrix and the corresponding orientation relationship (OR) was revealed as $(011)_\eta$//$(1122)_{Mg}$, $[100]_\eta$ deviated by 5.7x10^{-4} from $[1010]_{Mg}$. Because of

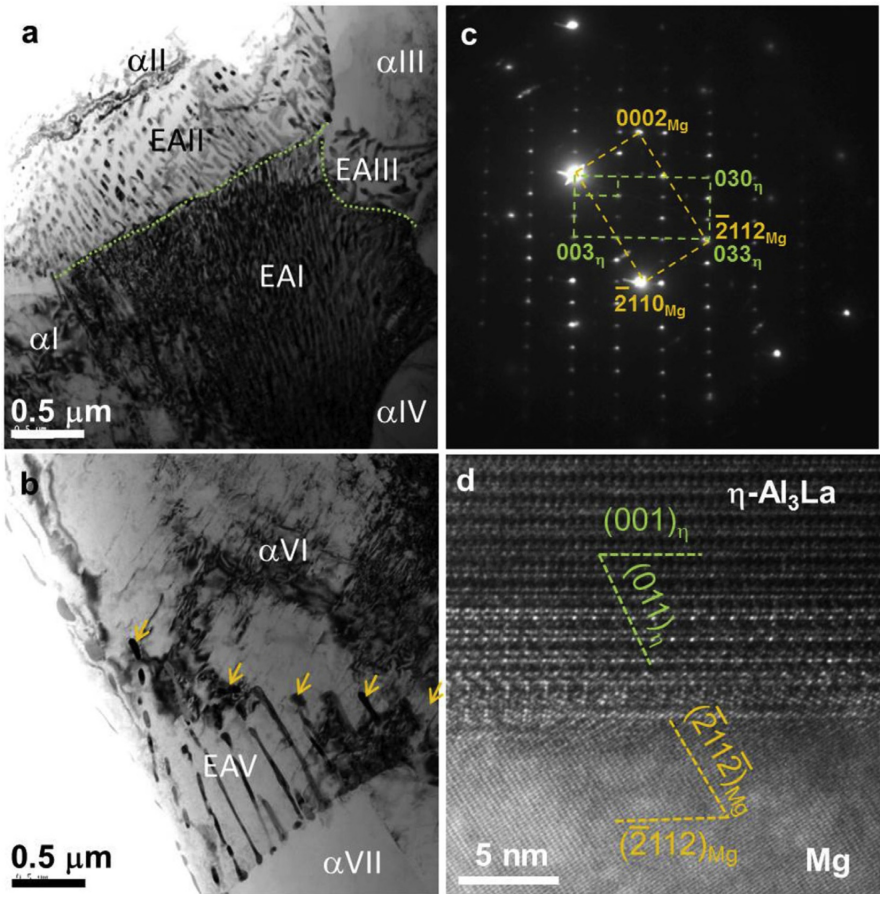

Figure 8: (a) and (b) BF-TEM images of the EAs, (c) SAED pattern from a fine η-Al_3La phase and (d) the interface between η-Al_3La and Mg matrix.

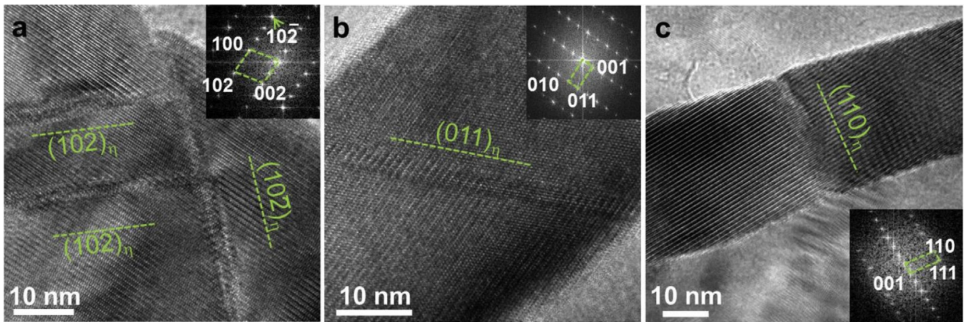

Figure 9: High magnified TEM images showing the formation of faults on (a) 102_η, (b) $(011)_\eta$ and (c) $(110)_\eta$ planes, respectively. The inserts are the corresponding fast Fourier transformed (FFT) patterns.

higher decohesion energy, coherent phase boundary is stronger than incoherent phase boundary. As a result, voids and fracture are relatively hard to take place at the coherent interface [59,60]. Furthermore, the above OR demonstrates that the $(001)_{\eta}$ plane is parallel to the $(1122)_{Mg}$ plane. Thus, the dislocation gliding on $(1122)_{Mg}$ plane can transfer to $(001)_{\eta}$ plane, providing driving force for slipping of MOTs or even forming new MOTs. This is the underlying reason why there are more MOTs in the η-Al_3La phase after large plastic deformation (see Supplementary Fig. 5e and f). However, <c + a> dislocation has to glide on multiple pyramidal $\{1122\}_{Mg}$ planes during plastic deformation. According to the above OR between η-Al_3La and Mg, $(011)_{\eta}$ plane is parallel to $(1122)_{Mg}$ plane, and $\{110\}_{\eta}$ and $\{102\}_{\eta}$ planes is approximately parallel to $(2112)_{Mg}$ and $(1212)_{Mg}$ planes, respectively. Thus, the <c + a> dislocation on pyramidal $\{1122\}_{Mg}$ planes would also transfer to $(011)_{\eta}$, $\{110\}_{\eta}$ or $\{102\}_{\eta}$ planes when bypassing η-Al_3La. Then, faults would form on the $(011)_{\eta}$, $\{110\}_{\eta}$ or $\{102\}_{\eta}$ planes. Indeed, such faults were observed in the specimens with large deformation such as shown in Fig. 9a-c. Finally, transferring of amounts of <c + a> dislocation through bypassing would lead to large misorientation angles between the bilateral matrixes of the η-Al_3La phase (see Supplementary Fig. 8). The drastic deformation of amounts of EAs near the grain boundaries could effectively coordinate the deformation between adjacent grains. Therefore, the high-strength of ALaM440 alloy is mainly attributed to the fine η-Al_3La particles which own coherent interface with Mg matrix. Also, the coherent η-Al_3La/Mg interface can effectively assist the pyramidal <c + a> dislocations bypassing the η-Al_3La particles, and then the fine layered Mg matrixes in EAs will coordinate the deformation among the adjacent grains. Thus, the ALaM440 alloy simultaneously accomplishes high-strength and high-ductility.

5 Conclusions

In this work, an alloy design concept based on controlling intermetallic phase components were proposed and conducted on Mg-Al-La system, and a new acicular intermetallic phase which owns highly similar morphology to the well-reported $Mg_{17}Al_{12}$ phase in Mg-Al-RE based alloys was found. According to the EDS analysis results and SAED pattern analysis, the new phase is η-Al_3La (a = 0.4437 nm, b = 0.4508 nm, c = 0.9772 nm, and β = 103.5°). Then, the atomic resolution HAADF STEM characterizations as well as DFT optimizations reveal the atomic configuration of η-Al_3La. Finally, the corresponding HAADF STEM and SAED simulations further confirmed the reasonability of the η-Al_3La structure revealed in this work. Furthermore, the developed alloy in this work has more excellent

strength-ductility balance and cost per-formance than all reported HPDC Mg alloys and the well-known HPDC A380 alloy.

Acknowledgements

This work was supported by the National Natural Science Foundation of China under grants no. 51701200, 11804030, 21521092 and 21601017, and the Project for Science & Technology Development of Jilin Province under grants no. 20180520004JH, 20160201100 4GX, 20170414001GH, and 20180520160JH. F.M., S.L. and Q.Y. acknowledge Wen-Zheng Zhang (Tsinghua University, China), Chunlin Chen (Tohoku University, Japan), and Yuichi Ikuhara (The University of Tokyo, Japan) for assistance in crystal structural analysis, TEM experiments and simulations.

References

1. Z. Wu, W.A. Curtin, The origins of high hardening and low ductility in magnesium, Nature 526 (2015) 62-67.

2. W.J. Joost, P.E. Krajewski, Towards magnesium alloys for high-volume automotive applications, Scr. Mater. 128 (2017) 107-112.

3. K. Guan, F. Meng, P. Qin, Q. Yang, D. Zhang, B. Li, W. Sun, S. Lv, Y. Huang, N. Hort, J. Meng, Effects of samarium content on microstructure and mechanical properties of Mg-0.5Zn-0.5Zr alloy, J. Mater. Sci. Technol. 35 (2019) 1368-1377.

4. M. Pekguleryuz, M. Celikin, Creep resistance in magnesium alloys, Int. Mater. Rev. 55 (2010) 197-217.

5. Q. Yang, S.-H. Lv, F.-Z. Meng, K. Guan, B.-S. Li, X.-H. Zhang, J.-Q. Zhang, X.-J. Liu, Jian Meng, Detailed structures and formation mechanisms of well-known $Al_{10}RE_2Mn_7$ phase in die-cast Mg-4Al-4RE-0.3Mn alloy, Acta Metall. Sin. (Engl. Lett.) 32 (2019) 178-186.

6. A.A. Luo, Recent magnesium alloy development for elevated temperature applications, Int. Mater. Rev. 49 (2004) 13-30.

7. Y. Lu, Q. Wang, X. Zeng, W. Ding, C. Zhai, Y. Zhu, Effects of rare earths on the microstructure, properties and fracture behavior of Mg-Al alloys, Mater. Sci. Eng. A 278 (2000) 66-76.

8. D. Choudhuri, S.G. Srinivasan1, Mark A. Gibson, Y. Zheng, D.L. Jaeger, H.L. Fraser, R. Banerjee, Exceptional increase in the creep life of magnesium rare-earth alloys due to localized bond stiffening, Nat. Commun. 8 (2017) 2000.

9. J.H. Zhang, S.J. Liu, R.Z. Wu, L.G. Hou, M.L. Zhang, Recent developments in high-strength Mg-RE-based alloys: focusing on Mg-Gd and Mg-Y systems, J. Magn. Alloys 6 (2018) 277-291.

10. X.-F. Gu, T. Furuhara, L. Chen, P. Yang, Solute clusters/enrichment at the early stage of ageing in Mg-Zn-Gd alloys studied by atom probe tomography, Acta Metall. Sin. (Engl. Lett.) 32 (2019) 187-193.

11. H. Westengen, P. Bakke, J.I. Skar, Magnesium Technology in the Global Age, CIM, Montreal, 2006, pp. 673-689.

12. J. Zhang, P. Yu, K. Liu, D. Fang, D. Tang, J. Meng, Effect of substituting cerium-rich mischmetal with lanthanum on microstructure and mechanical properties of die-cast Mg-Al-RE alloys, Mater. Des. 30 (2009) 2372-2378.

13. J. Zhang, K. Liu, D. Fang, X. Qiu, D. Tang, J. Meng, Microstructure, tensile properties, and creep behavior of high-pressure die-cast Mg-4Al-4RE-0.4Mn (RE = La, Ce) alloys, J. Mater. Sci. 44 (2009) 2046e-054.

14. S.M. Zhu, T.B. Abbott, M.A. Gibson, J.F. Nie, M.A. Easton, Age hardening in die-cast Mg-Al-RE alloys due to minor Mn additions, Mater. Sci. Eng. A 656 (2016) 34-38.

15. Q. Yang, F. Bu, F. Meng, X. Qiu, D. Zhang, T. Zheng, X. Liu, J. Meng, The improved effects by the combinative addition of lanthanum and samarium on the microstructures and the tensile properties of high-pressure die-cast Mg-Al-based alloy, Mater. Sci. Eng. A 628 (2015) 319-326.

16. S. Li, L. Qi, T. Zhang, J. Zhou, H. Li, Interfacial microstructure and tensile properties of carbon fiber reinforced Mg-Al-RE matrix composites, J. Alloys Compd. 663 (2016) 686-692.

17. T. Rzychon, A. Kielbus, L. Litynska-Dobrzynska, Microstructure, microstructural stability and mechanical properties of sand-cast Mg-4Al-4RE alloy, Mater. Char. 83 (2013) 21-34.

18. J. Zhang, M. Zhang, J. Meng, R. Wu, D. Tang, Microstructures and mechanical properties of heat-resistant high-pressure die-cast Mg-4Al-xLa-0.3Mn (x = 1, 2, 4, 6) alloys, Mater. Sci. Eng. A 527 (2010) 2527-2537.

19. J. Zhang, Z. Leng, M. Zhang, J. Meng, R. Wu, Effect of Ce on microstructure, mechanical properties and corrosion behavior of high-pressure die-cast Mg-4Al-based alloy, J. Alloys Compd. 509 (2011) 1069-1078.

20. J. Zhang, K. Liu, D. Fang, Xin Qiu, P. Yu, D. Tang, J. Meng, Microstructures, mechanical properties and corrosion behavior of high-pressure die-cast Mg-4Al-0.4Mn-xPr (x = 1, 2, 4, 6) alloys, J. Alloys Compd. 480 (2009) 810-819.

21. J. Zhang, J. Wang, X. Qiu, D. Zhang, Z. Tian, X. Niu, D. Tang, J. Meng, Effect of Nd on the microstructure, mechanical properties and corrosion behavior of die-cast Mg-4Al-based alloy, J. Alloys Compd. 464 (2008) 556-564.

22. Q. Yang, K. Guan, X. Qiu, D. Zhang, S. Lv, F. Bu, Y. Zhang, X. Liu, J. Meng, Structures of Al_2Sm phase in a high-pressure die-cast Mg-4Al-4Sm-0.3Mn alloy, Mater. Sci. Eng. A 675 (2016) 396-402.

23. Q. Yang, F. Bu, X. Qiu, Y. Li, W. Li, W. Sun, X. Liu, J. Meng, Strengthening effect of nano-scale precipitates in a die-cast Mg-4Al-5.6Sm-0.3Mn alloy, J. Alloys Compd. 665 (2016) 240-250.

24. S. Zhu, M.A. Easton, T.B. Abbott, M.A. Gibson, J.-F. Nie, The influence of individual rare earth elements (La, Ce, or Nd) on creep resistance of die-cast magnesium alloy AE44, Adv. Eng. Mater. 18 (2016) 932-937.

25. C. Wong, M.J. Styles, S. Zhu, D. Qiu, S.D. McDonald, Y. Zhu, M.A. Gibson, T.B. Abbott, $(Al,Mg)_3La$: a new phase in the Mg-Al-La system, Acta Crystallogr. 74 (2018) 370-375.

26. S. Lv, Y. Li, F. Meng, Q. Duan, Q. Yang, X. Liu, J. Meng, Thermodynamic stability of $Mg_{17}Al_{12}$ intermetallic compounds from first-principles calculations, Comput. Mater. Sci. 131 (2017) 28-34.

27. A.H. Gomes de Mesuita, K.H.J. Buschow, The crystal structure of so-called αa-$LaAl_4$ (La_3Al_{11}), Acta Crystallogr. 22 (1967) 497-601.

28. G. Pettersen, H. Westengen, R. Hoier, O. Lohne, Microstructure of a pressure die cast magnesium-4wt.% aluminium alloy modified with rare earth additions, Mater. Sci. Eng. A 207 (1996) 115-120.

29. CrystalMaker Software Ltd, Oxford, England, http://www.crystalmaker.com.

30. P. Villars, K. Cenzual, Pearson's Crystal Data: Crystal Structure Database for Inorganic Compounds, ASTM International, 2010.

31. C. Koch, Determination of Core Structure Periodicity and Point Defect Density along Dislocations, Ph.D. Thesis, Arizona State University, USA, 2002.

32. G. Kresse, J. Furthmuller, Efficient iterative schemes for ab initio total-energy calculations using a plane-wave basis set, Phys. Rev. B 54 (1996) 169-186.

33. J.P. Perdew, K. Burke, M. Ernzerhof, Generalized gradient approximation made simple, Phys. Rev. Lett. 77 (1996) 3865-3868.

34. P.E. Blochl, Projector augmented-wave method, Phys. Rev. B Condens. Matter 50 (1994) 17953.

35. G. Kresse, J. Joubert, From ultrasoft pseudopotentials to the projector augmented-wave method, Phys. Rev. B 59 (1999) 1758-1775.

36. S.M. Zhu, M.A. Gibson, M.A. Eastona, J.F. Nie, The relationship between microstructure and creep resistance in die-cast magnesium-rare earth alloys, Scr. Mater. 63 (2010) 698-703.

37. S. Gavras, M.A. Easton, M.A. Gibson, S. Zhu, J.-F. Nie, Microstructure and property evaluation of high-pressure die-cast Mg-La-rare earth (Nd, Y or Gd) alloys, J. Alloys Compd. 597 (2014) 21-29.

38. T. Rzychon, A. Kielbusa, J. Cwajna, J. Mizera, Microstructural stability and creep properties of die casting Mg-4Al-4RE magnesium alloy, Mater. Char. 60 (2001) 1107-1113.

39. S.M. Zhu, M.A. Gibson, J.F. Nie, M.A. Easton, T.B. Abbott, Microstructural analysis of the creep resistance of die-cast Mg-4Al-2RE alloy, Scr. Mater. 58 (2008) 477-480.

40. R. Krakow, D.N. Johnstone, A.S. Eggeman, D. Hunert, M.C. Hardy, C.M.F. Rae, P.A. Midgley, On the crystallography and composition of topologically close-packed phase in ATI 718Plus, Acta Mater. 130 (2017) 271-280.

41. Y. Ai, C.P. Luo, J. Liu, Twinning of CaMgSi phase in a cast Mg-1.0Ca-0.5Si-0.3Zr alloy, Acta Mater. 55 (2007) 531-538.

42. C. Liu, H. Chen, N. Wilson, J.-F. Nie, Twin-like fault in Mg-9.8 wt.%Sn alloy, Scr. Mater. 155 (2018) 89-93.

43. M. Easton, S. Zhu, M. Gibson, T. Abbott, H.Q. Ang, X. Chen, N. Birbilis, G. Savage, Performance evaluation of high-pressure die-cast magnesium alloys, in: K.N. Solanki, D. Orlov, A. Singh, N.R. Neelameggham (Eds.), Magnesium Technology, the Minerals, Metals & Materials Series, Springer, 2017, pp. 123-128.

44. S.M. Zhu, M.A. Easton, T.B. Abbott, J.F. Nie, M.S. Dargusch, N. Hort, M.A. Gibson, Evaluation of magnesium die-casting alloys for elevated temperature applications: microstructure, tensile properties, and creep resistance, Metall. Mater. Trans. A 46 (2015) 3543-3554.

45. Z. Leng, J. Zhang, M. Zhang, J. Meng, R. Wu, Microstructures and mechanical properties of heat-resistant high-pressure die-cast Mg-4Al-6RE-0.3Mn (RE = La, Ce, Pr, Nd, wt.%) alloys, Mater. Sci. Forum 686 (2011) 265-270.

46. S. Gavras, S.M. Zhu, J.F. Nie, M.A. Gibson, M.A. Easton, On the microstructural factors affecting creep resistance of die-cast Mg-La-rare earth (Nd, Y or Gd) alloys, Mater. Sci. Eng. A 675 (2016) 65-75.

47. H.Q. Ang, T.B. Abbott, S. Zhu, C. Gu, M.A. Easton, Proof stress measurement of die-cast magnesium alloys, Mater. Des. 112 (2016) 402-409.

48. M. Easton, M.A. Gibson, S. Zhu, T. Abbott, J.F. Nie, C.J. Bettles, G. Savage, Development of magnesium-rare earth die-casting alloys, in: D. Orlov, V. Joshi, K. Solanki, N.R. Neelameggham (Eds.), Magnesium Technology, the Minerals, Metals & Materials Series, Springer, 2018, pp. 329-336.

49. Z. Hu, L. Wan, S. Wu, H. Wu, X. Liu, Microstructure and mechanical properties of high strength die-casting Al-Mg-Si-Mn alloy, Mater. Des. 46 (2013) 451-456.

50. G. Timelli, F. Bonollo, The influence of Cr content on the microstructure and mechanical properties of AlSi9Cu3(Fe) die-casting alloys, Mater. Sci. Eng. A 528 (2010) 273-282.

51. M.S. Dargusch, K. Pettersen, P. Bakke, K. Nogita, A.L. Bowles, G.L. Dunlop, Microstructure and mechanical properties of high pressure die cast magnesium alloy AE42 with 1% strontium, Int. J. Cast Metals Res. 17 (2004) 170-173.

52. P. Bakke, A.L. Bowles, H. Westengen, Elevated temperature alloys - Paths for further performance gains in AE44, in: K.U. Kainer (Ed.), Magnesium: Proceedings of the 7th International Conference Magnesium Alloys and Their Applications, WILEYVCH Verlag Gmbh, Weinheim, 2007, pp. 55-66.

53. N. Mo, Q. Tan, M. Bermingham, Y. Huang, H. Dieringa, N. Hort, M.X. Zhang, Current development of creep-resistant magnesium cast alloys: a review, Mater. Des. 155 (2018) 422-442.

54. A.A. Luo, M.P. Balogh, B.R. Powell, Creep and microstructure of magnesium-aluminum-calcium based alloys, Metall. Mater. Trans. A 33 (2002) 567-574.

55. T.H. Courtney, Mechanical Behavior of Materials, Waveland, Long Grove, 2005.

56. D. Hull, D.J. Bacon, Introduction to Dislocations, fifth ed., Elsevier, 2011.

57. S.Q. Zhu, Simon P. Ringer, On the role of twinning and stacking faults on the crystal plasticity and grain refinement in magnesium alloys, Acta Mater. 144 (2018) 365-375.

58. H. Pan, G. Qin, Y. Huang, Y. Ren, X. Sha, X. Han, Z.-Q. Liu, C. Li, X. Wu, H. Chen, C. He, L. Chai, Y. Wang, J.-F. Nie, Development of low-alloyed and rare-earth-free magnesium alloys having ultra-high strength, Acta Mater. 149 (2018) 350-363.

59. Z. Zhang, W. Pantleon, Response of oxide nanoparticles in an oxide dispersion strengthened steel to dynamic plastic deformation, Acta Mater. 149 (2018) 235-247.

60. R. Goswami, N. Bernstein, Effect of interfaces of grain boundary Al_2CuLi plates on fracture behavior of Al-3Cu-2Li, Acta Mater. 87 (2015) 399-410.